RSC Advances

Simple approach to advanced binder-free nitrogen–doped graphene electrode for lithium batteries

SCHOLARONE™
Manuscripts

Graphical abstract

Simple approach to advanced binder-free nitrogen-doped graphene electrode for lithium batteries
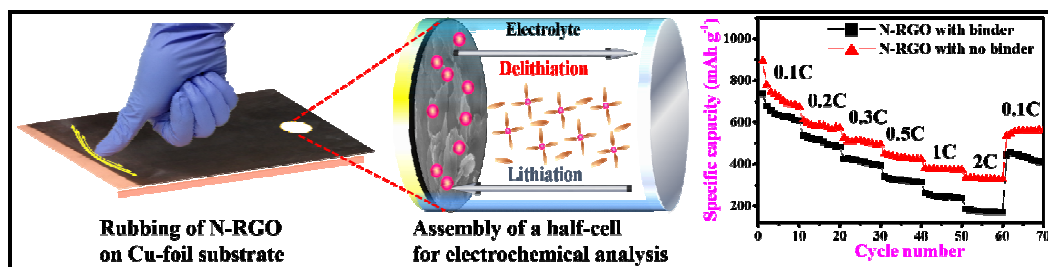
Current binder-free nitrogen-doped reduced graphene oxide (N-RGO) electrode imparts reduced electrode resistance and thus results in an excellent rate capability and high LIB performance. This method is not only highly reproducible and successful, but also easy to scale-up for commercial application.

RSC Advances

PAPER

Simple approach to advanced binder-free nitrogen-doped graphene electrode for lithium batteries

Hyean-Yeol Park, Kiran Pal Singh, Dae-Soo Yang and Jong-Sung Yu[*]

A simple binder-free synthesis approach of just rubbing nitrogen-doped reduced graphene oxide (N-RGO) powder on mechanically grinded Cu-foil substrate with rough surface is proposed for lithium ion battery (LIB). The nitrogen content of N-RGO is found to be 2.1 wt %. The binder-free N-RGO electrode shows excellent reversible capacity of 551 mA h g^{-1} as compared to 433 mA h g^{-1} of binder-added N-RGO electrode at a current density of 50 mA g^{-1} after 100 cycles. The process is not only highly reproducible and successful, but also results in high LIB performance, proposing ease scaling-up of such electrode for commercial application.

Introduction

With the growing demand to incorporate mobility into technology, lithium ion batteries (LIBs) serve as the most important power source for portable electronics and are also identified as a promising power solution for future electric vehicles. However, development of LIBs is now held-up by the graphite anodes due to their limited specific capacity (372 mA h g^{-1}), and poor rate capability.[1-5] As such, novel anode materials to achieve higher capacities without compromising the cyclability have become the subject of a thorough research worldwide.[6,7] Among the emerging materials, graphene has emerged out as a new promising materials owing to its superior properties such as great mechanical strength, excellent chemical and electrochemical stability and large specific surface area.[8-10]

Furthermore, incorporation of heteroatoms can tune the electronic structure of graphene, resulting in its improved electrochemical performance in many electrochemical devices.[11-14] There are various reports on the synthesis and assembly of heteroatom-doped graphene electrode.[12,15] The mode of material assembly on substrate is a significant step, determining the performance of an electrochemical device.

For efficient cell assembly, polyvinylidene fluoride (PVDF) is being used as a binder to certify good geometric integrity and good adhesion to the current collector.[16] However, adoption of a binder in the electrode complicates the electrode fabrication process and decreases the accessible specific area of the active

materials, which potentially declines effective lithium ion transport and cycling lifetime by introducing side reactions between the binder and electrolyte.[17] On the other hand, binder-free configuration can allow direct conductive pathways between active material and current collector, which can be beneficial for the effective charge transfer.[18,19] Hence, the binder-free configuration is not only simple, but also can efficiently satisfy objective of increasing energy and power density. Therefore, to increase the overall performance of the electrode system it is of paramount importance to find an alternative to the ubiquitously used binders.

Copper (Cu)-foil usually used for electrical contact surface is widely employed as an anode current collector for LIB due to its high stability at low potential, low price and good electrical conductivity. However, the normal Cu-foil in its natural state provides smooth surface. This makes it quite difficult to directly deposit materials, such as graphene, due to the lower adhesion provided by the smooth surface of Cu-foil.[20] Therefore, a type of Cu-foil prepared by mechanical grinding of surface in order to increase surface roughness and surface area is used for better adhesion of the active material.[21-23] The grinded Cu-foil can form an ideal surface for the deposition of exfoliated graphene layers, and hence make it suitable for the efficient coating of nitrogen-doped reduced graphene oxide (N-RGO) on the Cu-foil substrate. Herein, we propose for the first time a simple and efficient solvent-free and binder-free method to fabricate efficient anode electrodes from N-RGO as active

material using the grinded Cu-foil substrate with rough surface as a current collector.

Experimental

Synthesis of N-RGO

Firstly, the GO was synthesized from the natural flake graphite using improved hummers method.[24] In brief, 9:1 mixture of concentrated H_2SO_4/H_3PO_4 was added to 3.0 g graphite flake and 18.0 g $KMnO_4$. The oxidation was then carried out by heating and stirring the solution mixture at 50 ºC for 12 h. After oxidation reaction, mixture was poured into a mixture solution of ice (~400 ml) and 30 % H_2O_2 (3.0 ml). The obtained solution was centrifuged for 1 h at 4000 rpm, and the supernatant was decanted away, leaving behind brown colored powder. Obtained powder was then washed repeatedly with the mixture of ethanol, HCl and water. Obtained powder was dried overnight at 60 ºC. 200 mg GO was dispersed in 200 mL of ethanol by sonication and used for further synthesis.

For the synthesis of nitrogen-doped reduced GO (N-RGO), we followed the thermal expansion route. GO suspension was dried in oven at 80 ºC. The obtained brown colored powder is then carbonized at 900 ºC with a ramp of 10 ºC min⁻¹ in ammonia atmosphere. After the thermal expansion a black colored light powder was obtained, suggesting the reduction of GO to N-RGO.

Fabrication of binder-free N-RGO electrode

A binder-free (BF) N-RGO electrode was prepared using commercially available grinded Cu-foil substrate (Nippon Foil Mfg. Co., Ltd.) with thickness of 10 μm as a current collector. It was reported that the commercial Cu-foil was prepared by grinding with abrasive sand papers (Norton, P1000) followed by diamond paste polishing (diameter: 1.0 μm) in order to increase surface roughness and surface area.[21,22] The commercial grinded Cu-foil was ultrasonically washed in ethanol and water before rubbing N-RGO powder. As shown in Fig. 1a, a binder-free N-RGO electrode was prepared by simply rubbing N-RGO powder as an anode material on the grinded Cu-foil substrate and then pyrolyzing at 800 ºC in N_2 atmosphere at a rate of 5 ºC min⁻¹ for 1 h. The final product was directly used as a binder-free and solvent-free anode electrode. Such rubbing with N-RGO leads to the coverage of a graphitic layer on the rough surface of the grinded Cu-foil substrate.

Materials characterization

Scanning electron microscopy (SEM) (Hitachi S-4700 operating at 30 kV) and transmission electron microscopy (TEM) (JEOL FE-2010 operating at 200 kV) were employed to investigate the microstructure of the materials. X-ray photoelectron spectroscopy (XPS) was obtained with an AXIS-NOVA (Kratos) X-ray photoelectron spectrometer using monochromatic Al Kα (150 W) source under base pressure of 2.6×10^{-9} Torr. The XPS analysis was carried out to determine the elemental compositions of N-RGO. The purity of the samples (i.e., GO, RGO, and N-RGO) was examined by X-ray diffraction (XRD) analysis with a Rigaku Smartlab X-ray diffractometer with CuK$_α$ radiation (l=1.5406 Å) operating at 40 kV and 30 mA. Raman spectrum was recorded by Nanofinder-30 with a He-Ne laser (1.017 mW, 631.81 nm) to understand the molecular structure of the carbon material. Nitrogen sorption isotherm of N-RGO was measured at -196 ºC on Micromeritics ASAP 2020 surface area and porosity analyzer after the carbon was degassed at 250 ºC to 20 mTorr for 12 h. The specific surface areas were determined from nitrogen adsorption using the Brunauer-Emmett-Teller (BET) equation. Total pore volume was determined from the amount of gas adsorbed at the relative pressure of 0.99, while the pore size distribution of materials was calculated from analysis of the adsorption isotherms by the Barrett-Joyner-Halenda (BJH) method.

Electrochemical measurement

The electrochemical performance of the N-RGO material as a proposed binder-free and solvent-free anode in LIB, has been investigated in typical coin cells (half-cells). The coin cells were laboratory-assembled using CR 2032-coin cells (Hohsen Corp., Japan) in an argon-filled glove box where moisture and oxygen concentrations were strictly limited to below 0.1 ppm. A pure lithium metal (purity, 99.9 % and 150 mm thick) was used as a reference electrode and counter electrode. For comparison, N-RGO electrode with PVDF binder was also prepared by spreading a mixture of N-RGO, acetylene black, and PVDF at a weight ratio of 8:1:1 in N-methyl-2 pyrrolidone solvent onto the identical grinded Cu-foil substrate. The pasted copper substrate with binder was dried at 80 ºC and used directly for the battery testing without high temperature heat treatment unlike in the case of binder-free electrode. For all the coin cells, 1.0 M $LiPF_6$ in ethylene carbonate (EC)/dimethyl carbonate (DMC) (v/v = 1:1, Soulbrain Pte. Ltd.) was used as an electrolyte, and Celgard 2400 membrane as a separator.

The binder-free N-RGO electrodes were directly assembled into a coin cell for electrochemical tests primarily involving constant current cycling tests. Cyclic voltammetry (CV) experiments were carried out using a computer controlled potentiostat ((Biologic VMP3) in the potential range of 0.01 - 3.0 V at the scan rate of 0.1 mV s⁻¹ at room temperature. The galvanostatic charge-discharge tests were carried out on a BaSyTec multichannel battery test system at a current density of 50 mA g⁻¹ (0.1 C) with a cutoff voltage of 0.01-3.0 V vs. Li/Li⁺ at room temperature as described in previous work.[25,26]

Electrical conductivity measurements based on four-point probe method were tested on Keithley model 6220 and model 2182A used as the DC current source and voltmeter, respectively. As shown in Fig. S5a of ESI†, the cell was made of a non-conducting teflon block carved into a hollow cylinder, which was covered by two metallic brass pistons, one as a base and the other as a lid, to which the pressure was applied. Fine powdered carbon sample was filled in the hollow teflon

chamber, which in turn was sealed using two brass pistons, and resistivity measurement was performed by increasing the applied pressure. Current was applied to the sample through the metallic pistons and voltage was measured across the two metallic probes placed in the middle of teflon block. The electrical conductivity of the samples was estimated using the formula;

$$\sigma = L/RA$$

where σ is the electrical conductivity, R is the resistance of the sample, A is the cross sectional area of the sample (0.126 cm^2) and L is the distance between the voltage probes (0.2 cm). While measuring the resistivity, pressure was applied to the metallic pistons by using steel plates of known weights.[27-29]

Electrochemical impedance spectroscopy measurements (EIS) were carried out in the frequency range from 100 kHz - 10 mHz with an amplitude of superimposed AC signal of 0.01 V.

Results and discussion

A binder-free anode electrode was prepared by a simple two-step process: (1) hand rubbing of N-RGO powder onto the partially grinded Cu-foil substrate with rough surface at room temperature without use of any solvent and binder, and (2) thermal treatment of the resulting N-RGO electrode for better material integration. Fig. 1a describes the fabrication of a binder-free electrode from N-RGO and grinded Cu-foil substrate in a half cell configuration and a schematic illustration of the operating principle of LIB. During the charging process, Li ions are extracted from the cathode, go through the electrolyte and separator and intercalate into the anode with N-RGO. Simultaneously, electrons are liberated from the cathode, go through the external circuit and are accepted by anode compounds. The reverse process occurs during the discharging process. Inset SEM images of Fig. 1a show the rough surface on the grinded Cu-foil substrate (blue line), which enables easy adhesion of the N-RGO powder, and surface structure of as-prepared binder-free N-RGO electrode (red line).

Fig. 1b and 1c show SEM and TEM images of N-RGO. The N-RGO exhibits a crumbled sheet-like structure, including many ultrathin sheets and exfoliated layers. More images can be seen in Fig. S1a and S1b of ESI† as well. Similar morphology is also obtained for undoped RGO as shown in Fig. S1c and S1d (ESI†). To analyse the morphology of deposited N-RGO, we have carried out the HR-TEM analysis as shown in Fig. 1d. The deposited N-RGO material is shown to possess multilayered graphene structure with layer numbers varying from 2 to 10. It can be surmised that after thermal reduction in ammonia atmosphere, graphitic sheet structure in GO get partially restored to possess multilayered graphene structure.[30,31] The morphologies of the grinded and un-grinded normal Cu-foils were also investigated by SEM, as shown in Fig. S1e and S1f of ESI†. The grinded Cu-foil substrate shows increased surface roughness and irregular grains after grinding with
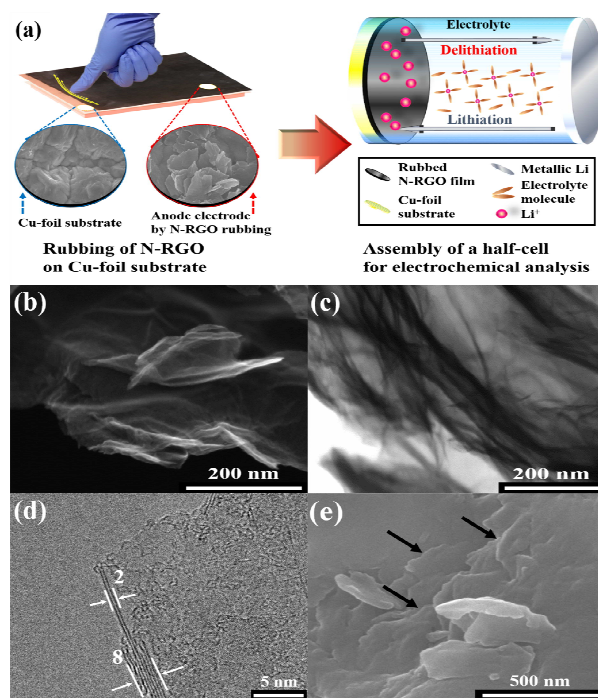

Fig. 1 (a) A schematic illustration of a simple fabrication process of binder-free electrode with N-RGO and partially grinded Cu film substrate and an assembly of the half-cell configuration. (b) SEM and (c) TEM images of N-RGO. (d) HR-TEM image of the N-RGO with different graphene sheets numbers. (e) Surface morphology of N-RGO deposited on the grinded Cu-foil substrate determined by SEM.

abrasive sand papers as compared to the un-grinded normal Cu-foil substrate. Hence, we propose this rough surface of the Cu-foil enables exfoliation and adhesion of the graphitic materials and provides a direct conducting path between graphene sheet and the surface of the grinded Cu-foil.[21] Fig. 1e shows that the fabricated binder-free N-RGO electrode produces stacked/compact structure, and possesses parallel grooves with a large portion of edge structures of graphene shown by the arrows.[32]

Fig. 2a shows X-ray diffraction (XRD) patterns of GO and N-RGO samples along with graphite. The disappearance of a sharp graphitic peak at 26.3° and appearance of a new peak at 9.43° indicates the successful conversion of graphite into GO without incorporation of any metallic impurities. However,
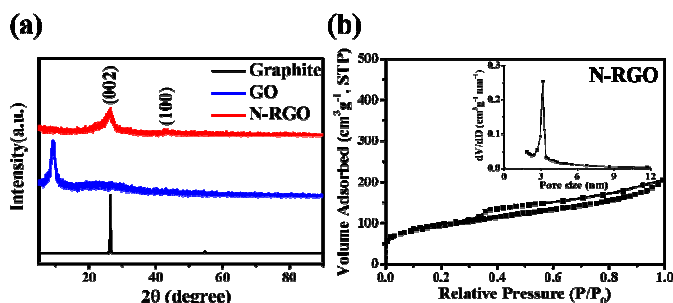
Fig. 2 (a) XRD patterns of original graphite powder, GO and N-RGO. (b) Nitrogen isotherms of N-RGO with an inset for pore size distribution curve.
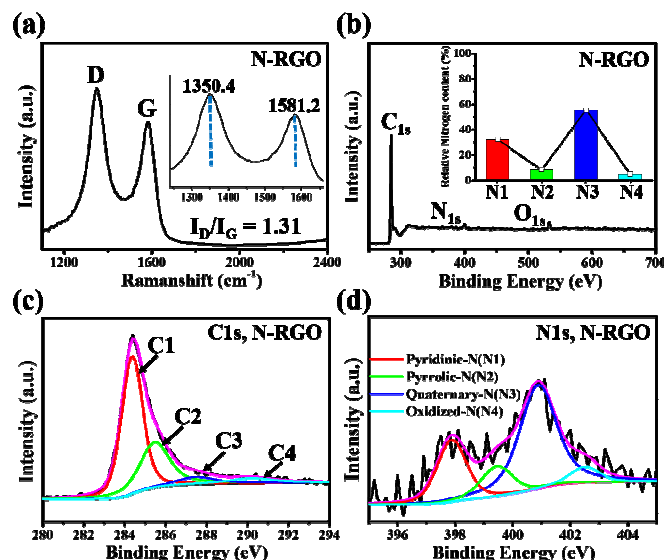
Fig. 3 (a) Raman spectra of N-RGO with an inset showing enlarged Raman spectra at 1250-1650 cm^{-1}, (b) XPS survey scan of N-RGO with an inset representing relative distribution of prominent N species for N-RGO, and deconvolution profiles of (c) C 1s and (d) N 1s spectra of N-RGO.

after thermal treatment, 002 peak again reappears at ~26.3°, but the peak becomes broader with a hump at 43.1° indicating the conversion of GO into the turbostratic carbon.[33] Nitrogen sorption isotherms indicate that the N-RGO has a surface area of 306.2 m^2 g^{-1} and a pore volume of 0.36 cm^3 g^{-1} with 3.2 nm pore size (inset of Fig. 2b), and reveals a type IV curve with the pronounced hysteresis loop typical of mesoporous materials.

Two characteristic Raman peaks at 1350.4 and 1581.2 cm^{-1}, which correspond to D and G band, respectively, can be seen in Fig. 3a. The G band arises from the zone center E_{2g} mode, corresponding to ordered sp^2-bonded carbon, whereas the D band is associated with the edges or disordered layers. Thus, the intensity ratio of the D and G band (I_D/I_G) provides a sensitive measure of the disorder of the graphitic layers.[34] The I_D/I_G value, which defines the level of disorderedness in the graphitic structure, is found to be around 1.31 for N-RGO, displaying highly disordered nature.[35]

X-ray photoelectron spectroscopy (XPS) was carried out to study the effect of N doping in the chemical environments of carbon. Fig. 3b shows XPS survey scan of N-RGO sample, and 3 prominent peaks corresponding to carbon, nitrogen and oxygen can be noticed, which signifies the successful incorporation of N (2.1 wt %) in N-RGO. Table S1 of ESI† shows elemental composition determined by XPS measurement of as-synthesized N-RGO sample.

C 1s spectrum of N-RGO sample was deconvoluted into four major peaks as can be seen in Fig. 3c. Peaks at ~284.4 eV and at ~285.6 eV are assigned to C1 (C=C sp^2-hybridized carbon) and C2 (sp^3 hybridized carbon), respectively. The small signals at higher binding energy (C3, ~287.6 eV and C4, ~290.2 eV) indicate the presence of C-O-C, C-N and/or C-O and physisorbed oxygen on the graphene, respectively.[36,37]

N 1s peak spectrum was deconvoluted into four N species corresponding to pyridinic-N (N1, ~397.9 eV), pyrrolic-N (N2, ~399.4 eV), quaternary-N (N3, ~400.9 eV), and oxidized-N (N4, ~402.5 eV) with relative N contents of 32.1 % pyridinic-N, 7.9 % pyrrolic-N, 55.2 % quaternary-N, and 4.8 % oxidized-N as seen in Fig. 3b and 3d. Due to the higher electronegativity of nitrogen (3.5) than carbon (3.0), the repulsive force between the Li ions can be compensated, which eventually helps enhancing the Li storage capacity in N-RGO.[38,39] Since binder-free N-RGO electrode was prepared by rubbing N-RGO powder on the grinded Cu-foil substrate followed by subsequent pyrolysis at 800 ºC in N$_2$ atmosphere for 1 h, XPS was also carried out to investigate the change of the chemical environments after pyrolysis. Fig. S2 of ESI† shows XPS survey scan and deconvolution profiles of N 1s of N-RGO-p sample obtained after pyrolysis. The relative amount of carbon increases with the decrease in relative oxygen and nitrogen quantity due to the pyrolysis, resulting in increase in C/O ratio. This increase in C/O ratio can improve the conductivity and Li-storage capacity of the N-RGO material, as with the restoration of carbon framework, the movement of ions on it improves. In addition, while relative pyridinic-N and pyrrolic-N content % decreased, relatively stable quaternary-N content % increased as summarized in Table S1 of ESI†.

Cyclic voltammetry (CV) of a binder-free N-RGO electrode was carried out at a scan rate of 0.1 mV s^{-1} between 0.01 and 3.0 V vs Li$^+$/Li for first sixth cycles to study electrochemical performance as shown in Fig. 4a. The measurement of a binder-free N-RGO electrode shows that Li$^+$ ions make reversible intercalation/de-intercalation into graphene layers. The first prominent reduction peak at about 0.7 V for both the N-RGO electrodes with and without binder is due to solid-electrolyte-interphase (SEI) film formation on the anodes, as evident from the CV plot and also from the first galvanostatic charge/discharge curves shown in Fig. 4b and 4c. This peak disappears during the 2nd cycle, which is due to the stable dense SEI film formation on the anode surface, which can separates the anode surface from the electrolyte. In Fig.4a, the second reduction peak appeared around 1.5 V shows the low Li ions diffusion inside the material and the formation of LiN$_x$ species on the surface of N-RGO during the first cycle, which may partly lead to the irreversible capacity in the first cycle.[40-42] No obvious changes were observed from the second to the sixth cycle of the CV plots, implying that not only no irreversible reactions were involved in after second cycle,[42] but also a binder-free N-RGO electrode has a good cycling performance, which is also consistent with the data derived from the cycling performance tests by the galvanostatic charge/discharge technique as shown in Fig. 5.

Fig. 4b and 4c represent the galvanostatic charge/discharge curves of binder-free and binder-added N-RGO cells at a constant current of 50 mA g^{-1} (0.1 C). A first voltage plateau around 0.7 V (vs. Li$^+$/Li), and a subsequent long continuous voltage drop down to 0.0 V are observed, which are indicative of the Li$^+$ intercalation/de-intercalation reactions and the formation of SEI film. The specific capacity and the
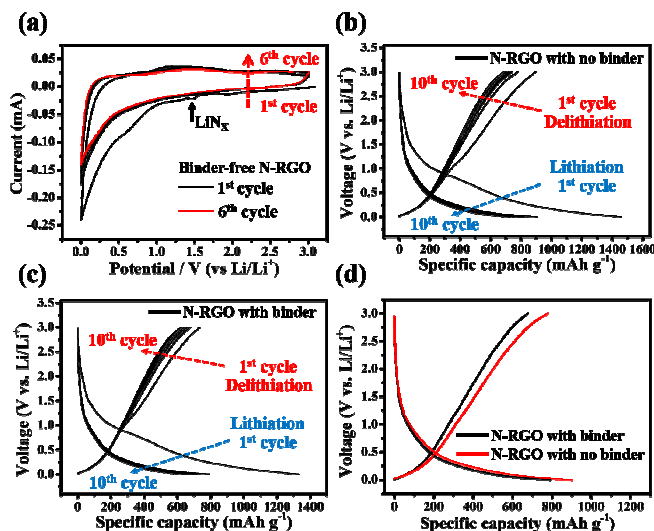
Fig. 4 (a) CV plots for binder-free N-RGO electrode for the first 6 cycles measured at a scan rate of 0.1 mV s^{-1} between 0.01 V to 3 V. Galvanostatic charge/discharge curves at 50 mA g^{-1} for (b) N-RGO with no binder and (c) N-RGO with binder. (d) Galvanostatic charge/discharge curves at 50 mA g^{-1} for N-RGO samples with binder and without binder for the second cycle.

irreversibility between the charge and discharge cycles become stabilized after the first few cycles. The first charging and discharging capacities of N-RGO powder cells with and without binder were found to be 1328, 736 mA h g^{-1} and 1457, 895 mA h g^{-1}, respectively, with an initial coulombic efficiency of 55 % and 61 %, and only a slight decrease in the specific capacity are observed after 2nd cycle, suggesting a good cycling performance for the binder-free N-RGO electrode.[43]

Fig. 4d shows galvanostatic charge/discharge curves obtained in the second charge/discharge cycle for the N-RGO samples with and without binder at a current density of 50 mA g^{-1}. These electrodes exhibit reversible Li storage capacity of ca. 778 (binder-free N-RGO) and 680 mA h g^{-1} (binder-added N-RGO), respectively. It is evident that discharge capacity for N-RGO without binder is much higher than that of N-RGO with binder. Additionally, binder-free N-RGO configuration allows enhanced kinetics of Li diffusion and transfer due to direct electronic transport pathways between grinded Cu-foil and N-RGO during cycling, which is expected to result in higher rate performance and cyclability.

Fig. 5a shows the galvanostatic cycling behaviour at 50 mA g^{-1} for the N-RGO electrodes. As compared to binder-added N-RGO electrode, the binder-free N-RGO electrode reveals not only a much higher initial reversible capacity, but also much higher Li storage capacity at the 100th cycle. The binder-free N-RGO electrode was found to be very stable up to the 100th cycle with a slight decrease in the reversible Li storage capacity. The N-RGO electrodes with and without binder retain a specific capacity of ca. 433, and 551 mA h g^{-1}, respectively after the 100th cycle. For the sake of comparison and to know the effect of binder-free configuration on RGO material, the cycling tests on undoped RGO electrodes with and without binder were also performed. As shown in Fig. S3c of ESI†, the binder-free RGO
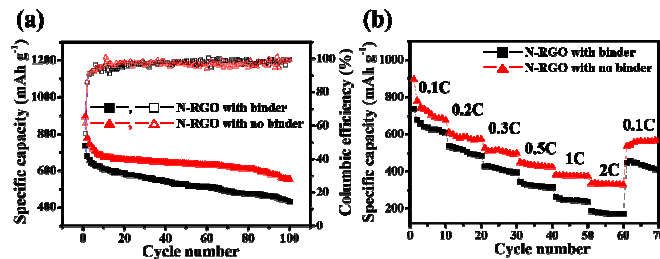

Fig. 5 (a) Comparison of cycling performance and coulombic efficiency at a specific current of 50 mA g^{-1}, and (b) comparison of rate performances of batteries at different current rates from 0.1 C to 2.0 C and then return to 0.1 C.

electrode reveals a higher specific capacity of ca. 394 mA h g^{-1} than RGO electrode with binder of ca. 303 mA h g^{-1}, respectively after the 100th cycle. This clearly indicates that good electrical contact between the electrode and current collector is realized by the direct deposition of N-RGO on the grinded Cu-foil substrate without use of binder.

Additionally, the binder-free N-RGO electrode demonstrates an excellent rate capability. The reversible discharge–charge storage capacities at different current densities are depicted in Fig. 5b. At rates from 0.1 C to 2.0 C, and its return to 0.1 C, the binder-free N-RGO electrode exhibited specific capacities of 895, 609, 524, 447, 380, 334, and 596 mA h g^{-1}, respectively. Even at a high current of 1000 mA g^{-1}, it delivers a higher capacity of 334 mA h g^{-1}. On the other hand, the rate performances of both undoped RGO electrodes with and without binder were also investigated in Fig. S3d. The binder-free RGO electrode exhibited specific capacities of 642, 464, 359, 282, 210, 152, and 403 mA h g^{-1}, respectively. Thus, the binder-free N-RGO electrode demonstrates much better cycle performance and rate capability both at low and high currents compared to the undoped RGO electrodes as well as the binder-added N-GRO. This further illustrates the exceptional capacity of this N-RGO electrode to keep its integrity without binder not only for long numbers of cycles, but also at high rates, and eventually leads to improved electrode energy density.[26,44]

To investigate whether the N-RGO electrodes with and without binder still retain electrical support, SEM images of those electrodes were shown before and after cycling to directly evaluate some changes in the morphology of deposited N-RGO during 100 cycles in Fig. S4 of ESI†. It can be seen in Fig. S4a that in N-RGO with binder, acetylene black and PVDF binder composite is homogenously deposited on the N-RGO surface before cycling performance. Compared with N-RGO with binder, the binder-free N-RGO electrode shows well deposited exfoliated graphene sheet, which provide a direct conducting path on the electrode as seen in Fig. S4c. However, after cycling performance, the traces of PVDF cannot be seen clearly, (Fig. S4b), which indicates that during electrochemical performance, PVDF might have decomposed, which can cause interference in the battery performance. Furthermore, there are large aggregation of active particles and some cracks in the N-RGO electrode, which will result in the electronic contact loss

and a less cyclability than before cycling. Similarly, due to the repeated lithiation and delithiation processes, formation of some amount of cracks and swelling in graphitic sheets were also observed in the binder-free N-ROG electrode, as seen in Fig. S4d, which decrease overall electrochemical performance.

Electrical conductivity plays an important role in enhancing the electron transfer and Li ion movement and hence is an important parameter to improve the LIB performance. We have measured the current-voltage characteristics of the N-RGO electrodes using four-point probe device (Fig. S5a of ESI†) and then plotted the conductivity against applied pressure to get the conductivity of binder-free and binder-added N-RGO powders. As can be seen in Fig. 6a, the binder-free N-RGO shows much higher conductivity as compared to that of binder-added N-RGO powder. This higher conductivity for the binder-free N-RGO electrode can help enhancing the Li storage capacity.[27]

To confirm the advantage of the constructed electrode, the electrochemical impedance spectroscopy (EIS) measurements were examined with the N-RGO cells, and the representative Nyquist impedance plots are shown in Fig. 6b. Fig. S5b of ESI† shows the equivalent circuit to fit the EIS. Both of the Nyquist plots show a well-defined semicircle in high to medium frequency followed by linear part towards lower frequency. The semicircle in the high frequency region includes electrolyte resistance (R_S) and charge transfer resistance (R_{CT}) occurring between active materials and liquid electrolyte. The straight line is attributed to the diffusion of lithium ions into electrode materials, or so-called Warburg diffusion (Z_W).[35,45] The result shows that the R_{CT} and Z_W values in the binder-free N-RGO cell are 56.2 and 12.4 Ω, which are lower than 75.1 and 17.3 Ω for the corresponding binder-added N-RGO cell. It is obvious that binder-free N-RGO configuration with high electrical conductivity generates much less resistance than binder-added N-RGO cell. The excellent conductivity of binder-free N-RGO can arouse long cyclability and high capacity at high rate current density. As expected, the internal resistance for binder-free N-RGO electrode is remarkably reduced because of the direct and efficient electrical pathways between active material and current collector as compared to N-RGO electrode with binder. Transfer of electrons can be promoted greatly during cycling, improving LIB performance of binder-free N-RGO electrode.[45]

The enhanced electrochemical performance of the binder-free N-RGO electrode can be explained through the following reasons: (1) the well-bonded N-doped RGO is expected to enhance the kinetics of lithium diffusion and transfer due to the introduction of a large number of topological defects on the graphene layers. (2) The assembled binder-free N-RGO electrode can provide efficient Li and electron transport pathways directly to the Cu-foil substrate during cycling. Both of them are beneficial for the electrochemical performance.

Conclusions

We have developed a simple alternative two-step route to the ubiquitously used binders using N-RGO on the partially
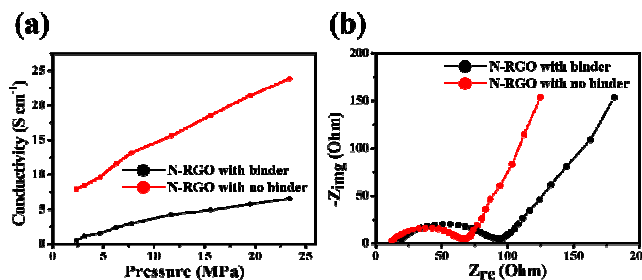

Fig. 6 (a) Conductivity *vs.* pressure curves of N-RGO with and without binder, and (b) Nyquist plots for N-RGO cells with and without binder.

grinded Cu-foil substrate; the deposition of N-RGO materials on the Cu-foil substrate with rough surfaces via a simple hand-rubbing followed by thermal treatment. This direct assembly of the N-RGO electrode was realized without use of any binder and solvent unlike in a conventional electrode-forming process. The outstanding long term cycle stability and rate capability of the binder-free N-RGO electrodes can be understood from the more facile electronic delivery and the larger electrical contact area.

Notes and references

a Department of Advanced Materials Chemistry, Korea University, 2511 Sejong-ro, Sejong, 339-700, Republic of Korea. E-mail: jsyu212@korea.ac.kr; Fax: +82-44-860-1331; Tel: + 82- 44-860-1494.

† Electronic Supplementary Information (ESI) available: [SEM, TEM, XPS, electrochemical tests, electrical conductivity device and equivalent EIS circuit of RGO materials]. See DOI: 10.1039/b000000x/

1   C.-X. Zu and H. Li, *Energy Environ. Sci.,* 2011, **4**, 2614-2624.
2   G. Jo, I. Choi, H. Ahn and M. J. Park, *Chem. Commun.,* 2012, **48**, 3987-3989.
3   M. Armand and J. M. Tarascon, *Nature,* 2008, **451**, 652-657.
4   P. G. Bruce, B. Scrosati and J.-M. Tarascon, *Angew. Chem., Int. Ed.,* 2008, **47**, 2930-2946.
5   J.-F. Wu, M.-Q. Xu, G.-C. Zhao, *Electrochem. Commun,* 2010, **12**, 175-177.
6   Y. Xiao, J. Zai, L. Tao, B. Li, Q. Han, C. Yu and X. Qian, *Phys. Chem. Chem. Phys.*, 2013, **15**, 3939-3945.
7.   Y. Liu, K. Huang, H. Luo, H. Li, X. Qi and J. Zhong, *RSC Adv.,* 2014, **4**, 17653-17659.

8. C. Wang, D. Li, C. O. Too and G. G. Wallace, *Chem. Mater.*, 2009, **21**, 2604-2606.

9. F. Razmjooei, K. P. Singh. M. Y. Song, and J.-S. Yu, *Carbon*, 2014, **78**, 257-267.

10. A. A. Balandin, S. Ghosh, W. Bao, I. Calizo, D. Teweldebrhan, F. Miao and C. N. Lau, *Nano Lett.*, 2008, **8**, 902-907.

11 D. Bhattacharjya, H.-Y. Park, M.-S. Kim, H.-S. Choi, S. Inamdar, and J.-S. Yu, *Langmuir*, 2014, **30**, 318-324.

12 D. Wei, Y. Liu, Y. Wang, H. Zhang, L. Huang and G. Yu, *Nano Lett.*, 2009, **9**, 1752-1758.

13 H. M. Jeong, J. W. Lee, W. H. Shin, Y. J. Choi, H. J. Shin, J. K. Kang and J. W. Choi, *Nano Lett.*, 2011, **11**, 2472-2477.

14 L. Qu, Y. Liu, J.-B. Baek and L. Dai, *ACS Nano*, 2010, **4**, 1321-1326.

15 X. Li, H. Wang, J. T. Robinson, H. Sanchez, G. Diankov and H. Dai, *J. Am. Chem. Soc.,* 2009, **131**, 15939-15944.

16 Y. Sun, J. Wang, B. Zhao, R. Cai, R. Ran and Z. Shao, *J. Mater. Chem. A.*, 2013, **1**, 4736-4746.

17 R. Black, S. H. Oh, J.-H. Lee, T. Yim, B. Adams and L. F. Nazar, *J. Am. Chem. Soc.*, 2012, **134**, 2902-2905.

18 C. Lu, W.-w. Liu, H. Li and B. K. Tay, *Chem. Commun.*, 2014, **50**, 3338-3340.

19 X. Li, J. Yang, Y. Hu, J. Wang, Y. Li, M. Cai, R. Li and X. Sun, *J. Mater. Chem.*, 2012, **22**, 18847-18853.

20 D. Mata, M. Amaral, A. J. S. Fernandes, F. J. Oliveira, P. M. F. J. Costa and R. F. Silva, *Carbon*, 2011, **49**, 2181-2196.

21 F. Lou, H. Zhou, F. Vullum-Bruer, T. D. Tran and D. Chen, *J. Energy. Chem.*, 2013, **22**, 78-86.

22 G. Xie, M. Forslund and J. Pan, *ACS Appl. Mater. Interfaces*, 2014, **6**, 7444-7455.

23 N. Kurra and G. U. Kulkarni, *Lab Chip*, 2013, **13**, 2866-2873.

24 D. C. Marcano, D. V. Kosynkin, J. M. Berlin, A. Sinitskii, Z. Sun, A. Slesarev, L. B. Alemany, W. Lu and J. M. Tour, *ACS Nano*, 2010, **4**, 4806-4814.

25 B. Fang, M.-S. Kim, J. H. Kim, S. Lim and J.-S. Yu, *J. Mater. Chem.*, 2010, **20**, 10253-10259.

26 M.-S. Kim, B. Fang, J. H. Kim, D.-S. Yang, Y. K. Kim, T.-S. Bae and J.-S. Yu, *J. Mater. Chem.*, 2011, **21**, 19362-19367.

27 M. Y. Song, H. Y. Park, D.-S. Yang, D. Bhattacharjya and J.-S. Yu, *ChemSusChem*, 2014, **7**, 1755-1763.

28 G. Zheng, L. Hu, H. Wu, X. Xie and Y. Cui, *Energy Environ. Sci.*, 2011, **4**, 3368-3373.

29 N. K. Chaudhari, M. Y. Song and J.-S. Yu, *Sci. Rept.*, 2014, **4**, 5221.

30 D. Long, W. Li, L. Ling, J. Miyawaki, I. Mochida and S.-H. Yoon, *Langmuir*, 2010, **26**, 16096-16102.

31 A. Muge and Y. J. Chabal, *J. Mater. Sci. Res.,* 2013, **2**, 101-112.

32 H. Sun, Y. Wang, S. Liu, L. Ge, L. Wang, Z. Zhu and S. Wang, *Chem. Commun.*, 2013, **49**, 9914-9916.

33 B. Fang, J. H. Kim, M.-S. Kim and J.-S. Yu, *Acc. Chem. Res.*, 2013, **46**, 1397-1406.

34 Z.-S. Wu, W. Ren, L. Xu, F. Li and H.-M. Cheng, *ACS Nano,* 2011, **5**, 5463-5471.

35 C. Zhang, L. Fu, N. Liu, M. Liu, Y. Wang and Z. Liu, *Adv. Mater.*, 2011, **23**, 1020-1024.

36 Y.-C. Lin, C.-Y. Lin and P.-W. Chiu, *Appl. Phys. Lett.*, 2010, **96**, 133110-133113.

37 Y. F. Li, Z. Zhou and L. B. Wang, *J. Chem. Phys.*, 2008, **129**, 104703-104707.

38 H. Wang, C. Zhang, Z. Liu, L. Wang, P. Han, H. Xu, K. Zhang, S. Dong, J. Yao and G. Cui, *J. Mater. Chem.*, 2011, **21**, 5430-5434.

39 X. Li, D. Geng, Y. Zhang, X. Meng, R. Li and X. Sun, *Electrochem. Commun,* 2011, **13,** 822-825.

40 H. Shimoda, B. Gao, X. P. Tang, A. Kleinhammes, L. Fleming, Y. Wu and O. Zhou, *Phys. Rev. Lett*, 2001, **88**, 015502.

41 L. G. Bulusheva, A. V. Okotrub, A. G. Kurenya, H. Zhang, H. Zhang, X. Chen and H. Song, *Carbon*, 2011, **49**, 4013-4023.

42 Y. Yang, K. Wu, R. Pang, X. Zhou, Y. Zhang, X. Wu, C. Wu, H. Wu and S. Guo, *RSC Adv.*, 2013, **3**, 14016-14020.

43 S. Zhu, C. Zhu, J. Ma, Q. Meng, Z. Guo, Z. Yu, T. Lu, Y. Li, D. Zhang and W. M. Lau, *RSC Adv.*, 2013, **3**, 6141-6146.

44 Q. Tang, Z. Shan, L. Wang and X. Qin, *Electrochim. Acta*, 2012, **79**, 148-153.

45 T. Hu, G. Xin, H. Sun, X. Sun, M. Yu, C. Liu and J. Lian, *RSC Adv.,* 2014, **4**, 1521-1525.